Polyurethane foam skeleton-based phase change hydrogel for efficient battery thermal management with favorable anti-vibration performance

Supporting Information

Chenggong Zhao,[a,b,c] Yifan Li, [a,,c,d*] Yicheng Liu, [a,c] Dahai Zhu, [a,c] Manping Ma,[e] Wei Yu [a,b,c*]

[a] School of Energy and Materials, Shanghai Key Laboratory of Engineering Materials Application and Evaluation, Shanghai Polytechnic University, Shanghai, 201209, China

[b] School of Electromechanical Engineering, Qingdao University of Science and Technology, Qingdao ,266061, China

[c] Shanghai Thermophysical Properties Big Data Professional Technical Service Platform, Shanghai Engineering Research Center of Advanced Thermal Functional Materials, Shanghai, 201209, China

[d] School of Materials Science and Engineering, East China University of Science and Technology, Shanghai, 200237, China

[e] School of Chemistry & Chemical Engineering, Shanghai Jiao Tong University, Shanghai, 200240, China

*Corresponding Author: Yifan Li, Email: liyf@sspu.edu.cn

Wei Yu, Email: yuwei@sspu.edu.cn

1. Optimization of PCH.

Various additives are experimented with to achieve the optimal thermal properties of PCH, such as phase transition temperature and enthalpy, as well as mechanical, thermal, and electrical properties. Table S1 displays the composition of the diverse PCHs, while their digital images are presented in Figure S1a. The role of PAA is to form gel networks and provide certain toughness, to facilitate the subsequent practical application in the thermal management of battery modules. The color of the original PCHs without thermal additives is white. The color gradually darkens as GO content increases. The alteration in thickness of the PEG/PAA composite under certain pressure is recorded, and the outcomes are displayed in Figure S1b. S3 and S4 exhibit relatively stable thickness upon increasing loading pressure. As an increased amount of PAA may influence the enthalpy of the composite, S3 is chosen for further experiments. The impact of thermally conductive additives on the thermal conductivity of PCH is demonstrated in Figure S1c. The original PCH (S3) has a lower thermal conductivity of 0.24 W/mK while the thermal conductivity of PCH with GO (composite PCH) is significantly improved. It is worth noting that the electrical conductivity of PCH with a higher loading percentage of GO fails to meet the common insulation requirement ($<10^{-6}$ cm), as demonstrated in Figure S1d. The BN doping could reduce the electrical conductivity of the composite PCH while S10 is selected for further investigation as it shows comparable thermal conductivity and satisfactory electrical conductivity, Figure S1e, which is used to prepare the subsequent PU-PCH plate. The phase transition properties are significant parameters for typical composite PCHs, and the results are

presented in Figure S1f. In general, the transition temperature varies little with the different components. The specific phase change parameters are summarized in Table S2. To differentiate the various sample components more clearly, the PCH without additives (S3) is labeled as the original PCH (*o*-PCH), while S10, which is utilized for further application, is labeled as the modified PCH (*m*-PCH). The uniformity of the thermal filler was further identified by SEM and EDS experiments, as shown in Figure S1 (g). According to the XRD results (Figure S1 h), the weaker BN peaks originate from the lower content of BN.

Table S1. The composition of the different PCHs.

Samples	Composition (g)			
	PEG	**PAA**	**GO**	**BN**
S1	60	12	0	0
S2	60	24	0	0
S3	60	30	0	0
S4	60	36	0	0
S5	60	30	0.6	0
S6	60	30	1.8	0
S7	60	30	3	0
S8	60	30	4.2	0
S9	60	30	1	2
S10	60	30	1.5	1.5
S11	60	30	2	1

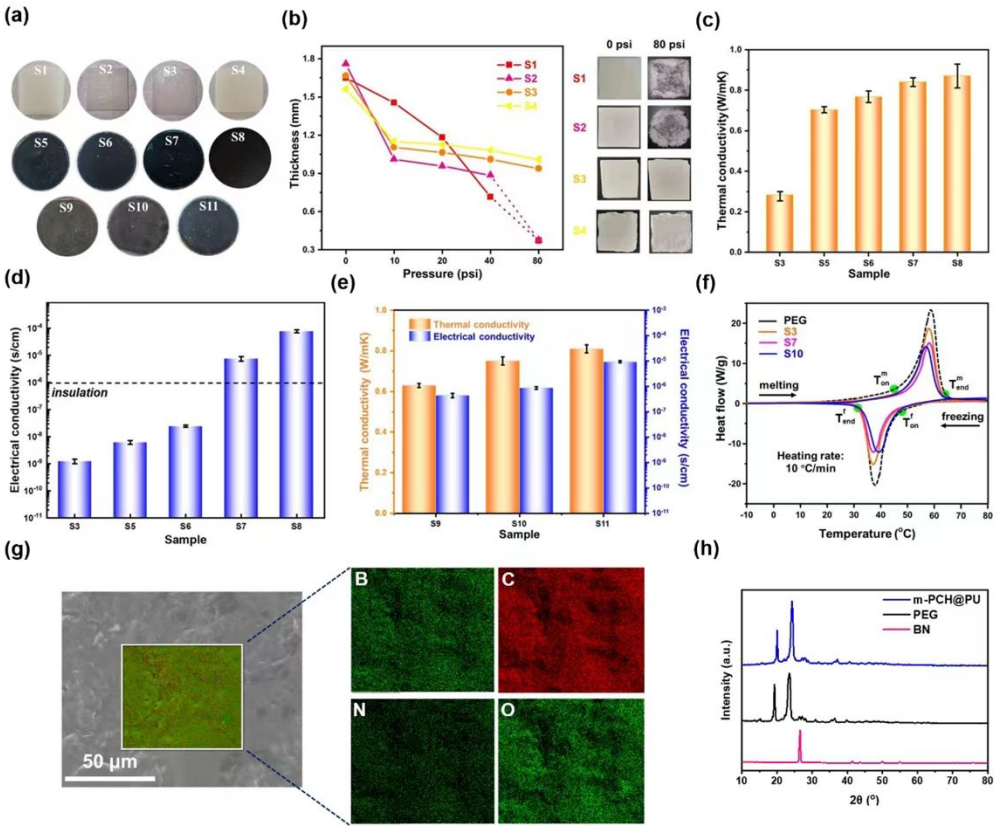

Figure S1. (a) Digital images of S1-S10; (b) thickness change of S1-S4 with corresponding shape change under an 80 psi pressure; (c) thermal conductivity and (d) electrical conductivity of the original PCH (S3) and composite PCHs (S5-S8); (e) thermal conductivity and electrical conductivity comparison of composite PCHs (S9-S11); (f) DSC curves of the original PEG and typical composite PCHs (S3, S7, S10); (g) the SEM and EDS of *m*-PCH@PU; (h) the XRD of BN, PEG and *m*-PCH@PU.

Table S2. Phase change parameters of the original PEG, S3, S7, and S10.

Samples	Melting Process			Freezing Process		
	T_{on}^{m} (°C)	T_{end}^{m} (°C)	ΔH_m (J/g)	T_{on}^{f} (°C)	T_{end}^{f} (°C)	ΔH_c (J/g)
PEG	47.32	63.14	183.20	51.68	33.47	160.46
S3	46.88	62.33	147.44	49.73	33.14	138.91
S7	45.91	61.67	124.13	49.68	33.20	113.69
S10	42.73	60.80	118.97	50.73	34.11	115.14

2. The surface roughness of samples

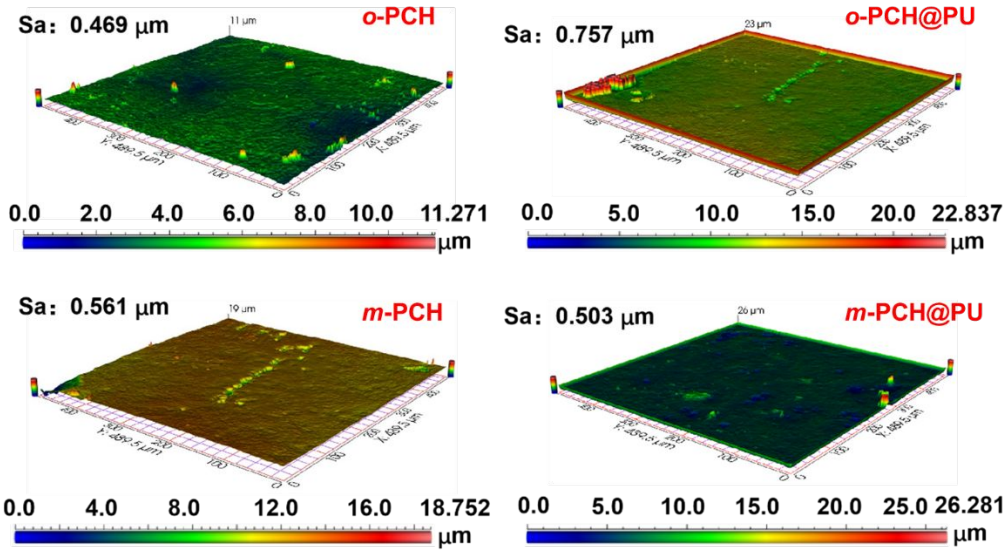

Figure S2. Surface roughness of the *o*-PCH, *m*-PCH, *o*-PCH@PU, and *m*-PCH@PU at room temperature. The arithmetic mean deviation (S_a) of the selected regional morphology of all samples is less than 0.8 μm, indicating a comparable interfacial heat conduction situation.

3. Testing system of TCR

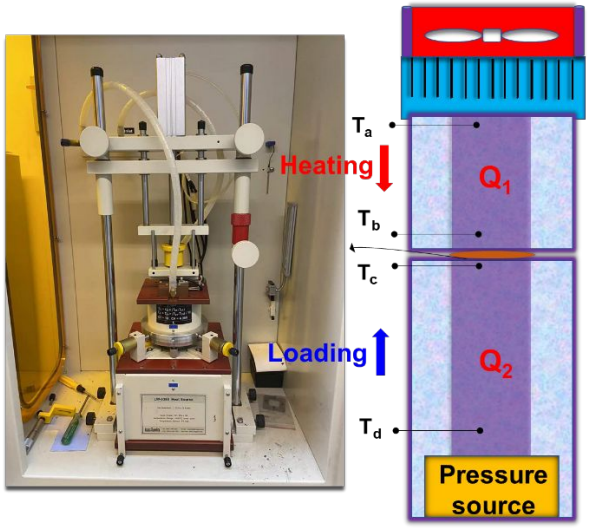

Figure S3. Testing platform setup for TCR.

The composites are placed between the hot and cold plates of the TCR measurement platform. According to Fourier's law, the heat flux of the hot side (Q_1) and the cold side (Q_2) is calculated by the following equations:

$$Q_1 = -kA\frac{T_a - T_b}{dx} \quad \text{(S1)}$$

$$Q_2 = -kA\frac{T_c - T_d}{dx} \quad \text{(S2)}$$

k is thermal conductivity, A is the area of heat conduction. T_a, T_b, T_c, and T_d are the measured temperature of the selected point. The average heat flux is used to calculate TCR (R_c):

$$R_c = \frac{T_b - T_c}{(Q_1 + Q_2)/2} \quad \text{(S3)}$$

4. Testing system of simulated temperature rise

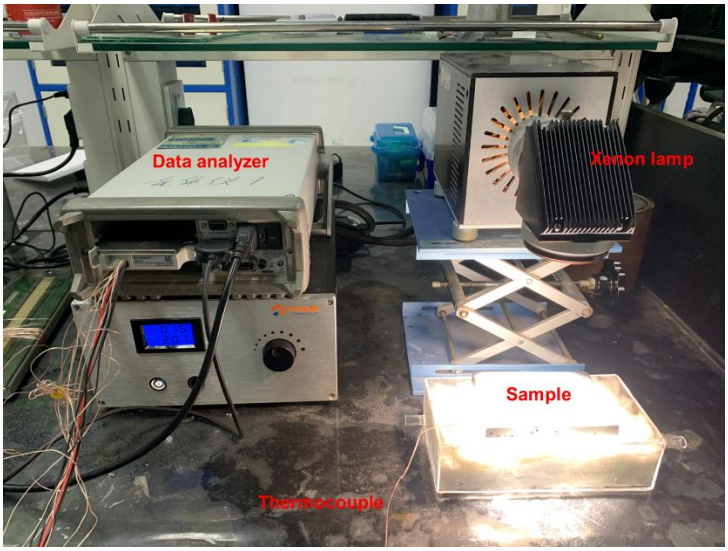

Figure S4. Experimental setup for the simulated temperature rise test.

5. testing system of battery performance

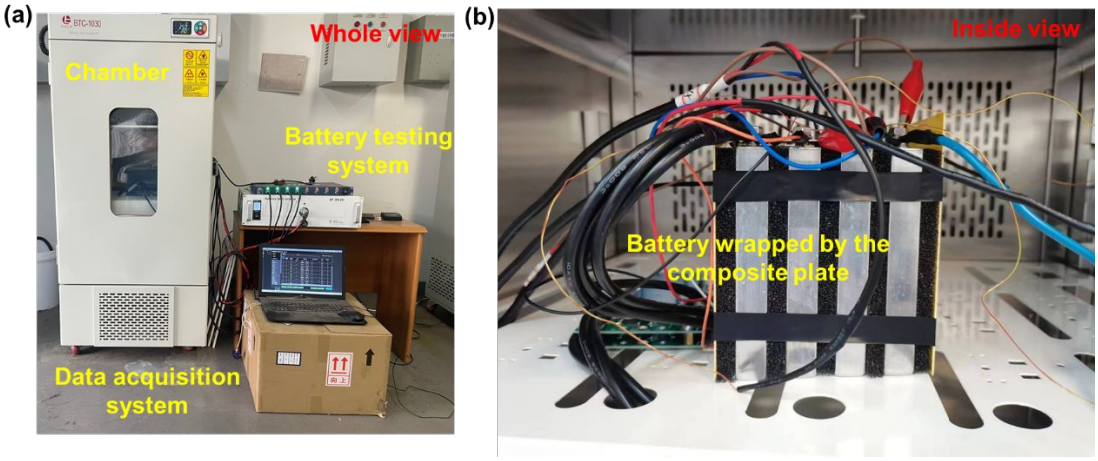

Figure S5. (a) Experimental setup for the entire battery testing system; (b) inside view of the chamber: schematic of the battery module wrapped by the composite plate.

6. Simulation details

6.1 Power battery heat generation model

The heat generation model of a LIB battery involves a multi-domain and multi-physics nature. Thermal analysis of the battery focuses on the temperature distribution at the battery's macroscopic length scale, while the electrochemical reaction, along with Li-ion transport, occurs at the microscopic atomic length scale. The Multi-Scale Multi-Domain (MSMD) approach with solvability for multiple physical processes is better suited for establishing the heat generation model of the battery. The thermal and electrical fields of the battery are solved in the Computational Fluid Dynamics (CFD) domain, considering the scale of the battery cell, through the following differential equations[1]:

$$q_{total} = \frac{\partial \rho C_p T}{\partial t} - \nabla \cdot (k \nabla T) = \sigma_+ |\nabla \emptyset_+|^2 + \sigma_- |\nabla \emptyset_-|^2 + \dot{q}_{ECh} + \dot{q}_{short} + \dot{q}_{abuse} \quad \text{(S4)}$$

σ_+ and $\emptyset_+$ are the electric conductivities and electric potentials for the positive, respectively; σ_- and $\emptyset_-$ are the electric conductivities and electric potentials for the negative electrodes, respectively; $\dot{q}_{ECh}$, $\dot{q}_{short}$, $\dot{q}_{abuse}$ are the electrochemical reaction heat, heat generation rate, and heat generation due to electrochemical reactions, battery internal short-circuit, and thermal runaway reactions. Battery electrical fields are solved in the CFD domain at the battery cell's scale using the following differential equations[1]:

$$\nabla \cdot (\sigma_+ \nabla \varphi_+) = - (j_{ECh} - j_{short}) \quad \text{(S5)}$$

$$\nabla \cdot (\sigma_{-} \nabla \varphi_{-}) = j_{ECh} - j_{short}$$

(S6)

φ_{+} and φ_{-} are phase potentials for the positive and negative electrodes; j_{ECh} and j_{short} are the current transfer rate due to electrochemical reactions and battery internal short-circuit. For normal operation, j_{short}, $\dot{q}_{short}$ and $\dot{q}_{abuse}$ are set to zero. Thus, Equations (S4)-(S6) can be simplified as[1]:

$$\frac{\partial \rho C_p T}{\partial t} - \nabla \cdot (k \nabla T) = \sigma_{+} |\nabla \emptyset_{+}|^2 + \sigma_{-} |\nabla \emptyset_{-}|^2 + \dot{q}_{ECh}$$

(S7)

$$\nabla \cdot (\sigma_{+} \nabla \varphi_{+}) = - j_{ECh}$$

(S8)

$$\nabla \cdot (\sigma_{-} \nabla \varphi_{-}) = j_{ECh}$$

(S9)

j_{ECh} and $\dot{q}_{ECh}$ can be calculated through electrochemical models. In this work, we solve this problem using the Newman, Tiedemann, Gu, and Kim (NTGK) model. NTGK model presents excellent comfortability for stable loads, which are generally controlled by the discharge current[1].

$$j_{ECh} = \frac{Q_{nominal}}{Q_{ref} Vol} Y[U - V]$$

(S10)

$Q_{nominal}$ represents the battery's total electric capacity in Ampere hours; Vol is the active zone's volume of a single battery; V is the cell voltage calculated by MSMD solution; Q_{ref} is the capacity of the battery that is used in experiments to obtain the

cell's original parameters Y and open circuit voltage U, which are associated with the depth of discharging[1].

$$U = \left(\sum_{n=0}^{5} a_n (DoD)^n\right) - C_2(T - T_{ref})$$

(S11)

$$Y = \left(\sum_{n=0}^{5} b_n (DoD)^n\right) exp\left[- C_1\left(\frac{1}{T} - \frac{1}{T_{ref}}\right)\right]$$

(S12)

C_1 and C_2 are the battery-specific NTGK model constants. The DoD can be obtained by solving the following Equation (S13)[1]:

$$DoD = \frac{Vol}{3600 Q_{nominal}} \int_0^t j dt \quad \text{(S13)}$$

Where j is the apparent current density (A/m^2).

$\dot{q}_{ECh}$ can be calculated by Equation (S14) in the NTGK model[1]:

$$\dot{q}_{ECh} = j_{ECh}\left[U - V - T\frac{dU}{dT}\right]$$

(S14)

6.2 Power battery heat transfer model

Heat transfer occurs primarily through conduction, convection, and radiation. In batteries, heat is primarily generated at the positive and negative poles as well as in the inner core. The heat generated in the battery core is transferred through the battery shell, phase change material, and the surrounding air. In this process, conduction and convection are the dominant modes of heat transfer, while radiation is negligible and can be disregarded.

6.3 Heat conduction

In a battery, the conduction of heat complies with Fourier's law. For any small volume element in the battery, the heat transfer process can be described by the three-dimensional unsteady heat diffusion equation:

$$\rho c\left(\frac{\partial T}{\partial t}\right) = \frac{\partial}{\partial x}\left(\lambda\frac{\partial T}{\partial x}\right) + \frac{\partial}{\partial y}\left(\lambda\frac{\partial T}{\partial y}\right) + \frac{\partial}{\partial z}\left(\lambda\frac{\partial T}{\partial z}\right) + q \quad \text{(S15)}$$

ρ is the battery density with the unit of Kg/m^3; c is the specific heat capacity of the battery; q is the heat generated per unit volume of the battery; λ is the thermal conductivity of the battery in x, y, and z directions; T is the temperature, and t is time. Considering λ as a constant, the heat generated during the charging and discharging of a battery plus the change of heat in three dimensions equals the net change of heat of a battery. For simplified calculations, the thermal physical property parameters were assumed to be constant, and the thermal conductivity was assumed to be isotropic in the x and y directions. As a result, Equation (S15) can be expressed in a simplified form:

$$\rho c\left(\frac{\partial T}{\partial t}\right) = \lambda_{(x,y)}\left(\frac{\partial^2 T}{\partial x^2} + \frac{\partial^2 T}{\partial y^2}\right) + \lambda_z\frac{\partial^2 T}{\partial z^2} + q \quad \text{(S16)}$$

$\lambda_{(x,y)}$ is the thermal conductivity in the x and y directions, and λ_z is the thermal conductivity in the z-direction.

6.4 Heat convection

Convection heat transfer can be calculated using Newton's law of cooling, as described by Equation (S17):

$$Q_{conv} = h \cdot A \cdot (T - T_f)$$

(S17)

Q_{conv} is convective heat transfer, h is convective heat transfer coefficient, T-T_f is the temperature difference between the object and the surrounding medium, T is the battery surface temperature, T_f is the temperature of the cooling medium, A is the area of convective heat transfer. The convective heat transfer coefficient h is related to the temperature difference between the fluid and the solid as well as the flow velocity and viscosity of the fluid. The heat transfer formula between the battery surface and the external fluid can be calculated by Newton's cooling law, Equations (S18)-(S20)[2]:

$$- \lambda_{(x,y)} \frac{\partial T}{\partial x} \Big/_{x = x_1} = h\left(T \Big/_{x = x_1} - T_f\right)$$

(S18)

$$- \lambda_{(x,y)} \frac{\partial T}{\partial y} \Big/_{y = y_1} = h\left(T \Big/_{y = y_1} - T_f\right)$$

(S19)

$$- \lambda_z \frac{\partial T}{\partial z} \Big/_{z = z_1} = h\left(T \Big/_{z = z_1} - T_f\right)$$

(S20)

6.5 Basic governing equations of fluid mechanics

The governing equations include the conservation of mass, momentum, and energy, described by the following equations[2]:

Mass conservation:

$$\frac{\partial(\rho u_x)}{\partial x} + \frac{\partial(\rho u_y)}{\partial y} + \frac{\partial(\rho u_z)}{\partial z} + \frac{\partial \rho}{\partial t} = 0$$

(S21)

$$\frac{\partial u_x}{\partial x} + \frac{\partial u_y}{\partial y} + \frac{\partial u_z}{\partial z} = 0 \quad \text{(Considering } \rho \text{ as a constant)} \qquad \text{(S22)}$$

Momentum conservation:

$$\frac{\partial(\rho u_x)}{\partial t} + \nabla(\rho u_x \vec{u}) = \rho f_x - \frac{\partial P}{\partial x} + \frac{\partial \tau_{xx}}{\partial x} + \frac{\partial \tau_{yx}}{\partial y} + \frac{\partial \tau_{zx}}{\partial z}$$

(S23)

$$\frac{\partial(\rho u_y)}{\partial t} + \nabla(\rho u_y \vec{u}) = \rho f_y - \frac{\partial P}{\partial y} + \frac{\partial \tau_{xy}}{\partial x} + \frac{\partial \tau_{yy}}{\partial y} + \frac{\partial \tau_{zy}}{\partial z}$$

(S24)

$$\frac{\partial(\rho u_z)}{\partial t} + \nabla(\rho u_z \vec{u}) = \rho f_z - \frac{\partial P}{\partial z} + \frac{\partial \tau_{xz}}{\partial x} + \frac{\partial \tau_{yz}}{\partial y} + \frac{\partial \tau_{zz}}{\partial z}$$

(S25)

Energy conservation:

$$\frac{\partial(\rho T)}{\partial t} + \frac{\partial(\rho u_x T)}{\partial x} + \frac{\partial(\rho u_y T)}{\partial y} + \frac{\partial(\rho u_z T)}{\partial z} = \frac{\partial}{\partial x}\left(\frac{\lambda \partial T}{c \partial x}\right) + \frac{\partial}{\partial y}\left(\frac{\lambda \partial T}{c \partial y}\right) + \frac{\partial}{\partial z}\left(\frac{\lambda \partial T}{c \partial z}\right) \quad \text{(S26)}$$

6.6 Verification of transient heat generation model of a single battery cell

A three-dimensional geometric model of the single battery was created using SpaceClaim software, with the pressure relief holes removed while retaining the positive and negative poles. The battery dimensions are 18 mm × 80 mm × 124 mm, with a pole diameter of 6 mm for both the positive and negative poles. Tetrahedral meshing was performed using the mesh tool in Workbench, and each part and surface of the battery was named. Import the partitioned mesh into Fluent and verify the absence of negative volume grids. Transient thermal simulation analysis was selected with a gravity field added. The gravitational acceleration was set as -9.81 $m \cdot s^{-2}$. The initial temperature was the same as the experimental test. Setting the energy equation and the standard viscosity model k-epsilon (2 eqn), and setting the thermal and physical parameters of each part. The basic parameters of the battery are provided in Table S3. When defining the heat source, we use the built-in heat generation rate model of Fluent

software for calculation. In the boundary conditions, the heat transfer adopts the convection heat transfer between the external environment and the battery surface, and the natural convection heat transfer coefficient is set at 5 W/m^2K. Because the heat exchange inside the battery pack is fluid-structure coupled heat transfer, the SIMPLE algorithm is chosen as the solver format to calculate the spatial discrete equation. At 2C (16 A) and 6 C (48 A) discharge conditions, set the time step to 1800 and 600, respectively, with step length to 1 second.

Table S3. Basic parameters of the battery.

Parameter	value
Size (mm^3)	80×124×18
Density ($kg \cdot m^{-3}$)	2100
Thermal conductivity at z-direction (W/mK)	28.4
Thermal conductivity at x,y-directions (W/mK)	25.1
Specific heat capacity (J/KgK)	1200
Nominal capacitance (Ah)	8
Nominal voltage (V)	3.2
Discharging cut-off voltage (V)	2
Charging cut-off voltage (V)	3.65
Internal resistance (mΩ)	≤1.3
Cathode material	$LiFeCoPO_4$
Anode material	Graphite
Electrolyte material	$C_3H_4O_3$

7. The Hybrid Pulse Power Characteristic (HPPC) method

Figure S6 illustrates the schematic diagram outlining the principle of the Hybrid Pulse Power Characteristic (HPPC) method. Initially, during the pulse discharge, the voltage experiences a sudden drop from U_0 to U_1 due to the cell's Ohmic resistance. Subsequently, the voltage gradually decreases to U_2, aligning with the cell's polarization reaction. Upon cessation of pulsed discharge, the voltage abruptly returns to its normal state.

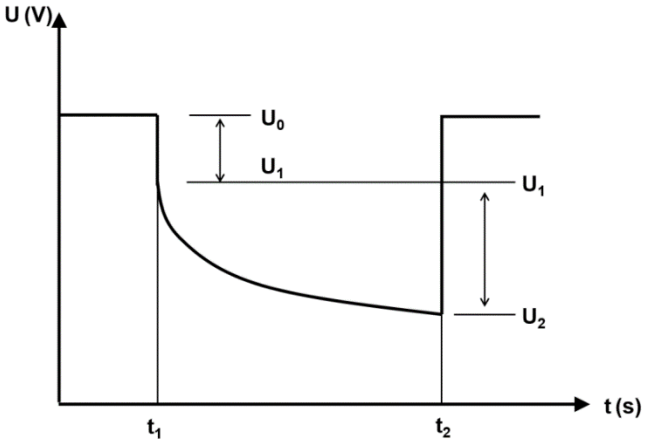

Figure S6. The schematic diagram of the principle of Hybrid Pulse Power Characteristic (HPPC) method.

The R corresponding to the SOC can be calculated by Equation (S27) using the records of U_0 and U_2 corresponding to each SOC during the pulse test[3].

$$R = \frac{U_0 - U_2}{I} \quad \text{(S27)}$$

U_0 and U_2 are the terminal voltage before and after pulse discharge, respectively. I is the discharge current.

The obtained R comprises two components: ohmic resistance and polarization internal resistance. In this study, these two components were treated collectively. To ensure higher accuracy, pulse measurements were taken after the release of every 10% SOC. The specific testing procedure is outlined as follows:

(1) Complete cell discharge: The cell was subjected to a constant temperature of 45 ℃ and 50% RH in an oven. After discharging the cell at a cross current of 4 A until the voltage ≤ 0.1 V, it was then kept idle for 1 h.

(2) Complete cell charging: The cell underwent charging at a constant current of 4 A until reaching the cut-off voltage of 3.65 V. It was then charged at a constant voltage until the current dropped to 0.4 A, indicating completion of the charging process with the SOC of 100%. Subsequently, the cell was kept idle for 1 h.

(3) Cell discharge at a constant current of 40 A was conducted for 10 s, and the resulting voltage change was recorded to calculate the R for the SOC of 100%. Subsequently, the cell was kept idle for 1 h.

(4) Cell discharge at a constant current of 40 A was carried out until reaching the SOC of ≤ 90%. The cell was then kept idle for 1 h.

(5) The R values corresponding to SOC ranging from 100% to 0% were obtained by iteratively repeating steps (3) and (4) for a total of 10 cycles, each time reducing the capacity by 10%.

8. References

(1) Hussain, M.; Khan, M. K.; Pathak, M. Thermal analysis of phase change material

encapsulated li-ion battery pack using multi-scale multi-dimensional framework. *Journal of Energy Storage* **2023,** 65, 107290. https://doi.org/10.1016/j.est.2023.107290.

(2) Singh, L. K.; Kumar, R.; Gupta, A. K.; Sharma, A. K.; Panchal, S. Computational study on hybrid air-PCM cooling inside lithium-ion battery packs with varying number of cells. *Journal of Energy Storage* **2023,** 67, 107649. https://doi.org/10.1016/j.est.2023.107649.

(3) Wu, Q.; Huang, R.; Yu, X. Measurement of thermophysical parameters and thermal modeling of 21,700 cylindrical battery. *Journal of Energy Storage* **2023,** 65, 107338. https://doi.org/10.1016/j.est.2023.107338.